

See discussions, stats, and author profiles for this publication at: <https://www.researchgate.net/publication/269185218>

# Mesoporous Alumina Films: Effect of Oligomer Formation Towards Mesostructural Ordering.

ARTICLE *in* LANGMUIR · DECEMBER 2014

Impact Factor: 4.46 · DOI: 10.1021/la503374n · Source: PubMed

---

READS

54

## 2 AUTHORS:



Anuradha Mitra

Jadavpur University

10 PUBLICATIONS 40 CITATIONS

[SEE PROFILE](#)



Goutam De

Central Glass and Ceramics Research Institute

132 PUBLICATIONS 2,131 CITATIONS

[SEE PROFILE](#)

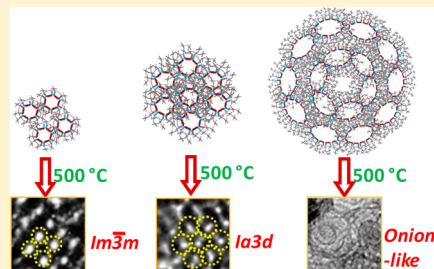
## Mesoporous Alumina Films: Effect of Oligomer Formation toward Mesosstructural Ordering

Anuradha Mitra and Goutam De\*

Nano-Structured Materials Division, CSIR—Central Glass and Ceramic Research Institute, 196, Raja S. C. Mullick Road, Kolkata 700032, India

### Supporting Information

**ABSTRACT:** Alumina films with  $I\bar{m}\bar{3}m$ ,  $Ia3d$ , and onion-like mesopores have been synthesized using a single sol composition derived from a modified alumina precursor (MAP), partial acetylacetone (acac) chelated aluminum secondary butoxide (ASB/acac = 1:0.5). We observed that MAP undergoes oligomerization with aging time and the differently aged MAP generates different micellar structures in the presence of P123 in alumina sols, and forms differently ordered mesostructured coatings. The time-dependent changes in the chemical nature of the MAP have been studied through ATR-FTIR spectroscopy. The nature of micellar transformations in the sols have been studied by transmission SAXS investigations. It has been observed that the size of the micelles gradually increases with time. On aging, MAP contains more bridging alkoxide groups with lesser hydrophilic characteristics; this reduces its interaction with the hydrophilic groups in the P123 micelle. Therefore, a mesostructure with low curvature is gradually formed in the sol due to the rigid nature of cross-linked MAP. Low angle XRD and TEM studies of the coatings obtained from the above sols have confirmed the generation of three distinctly different types of ordered mesoporous arrangements after heat treatments. The time-induced mesophase transformation mechanism has been proposed based upon the experimental results. The study reveals transformation of a modified Al alkoxide solution with respect to time and its successful use to obtain mesoporous alumina films of different ordered structures on glass.



### 1. INTRODUCTION

Mesoporous alumina is a very important material due to its potential applications as an adsorbent for removal of pollutants,<sup>1</sup> industrial catalysts,<sup>2–4</sup> and support material.<sup>5–9</sup> Recently, we have demonstrated that the presence of well-connected and accessible pores in ordered mesoporous alumina film enhances its reactivity in the decomposition of aqueous  $KMnO_4$  solution compared to the disordered analogue.<sup>2</sup> This clarifies the importance of periodic organization of mesopores in alumina films. Therefore, soft-template synthesis of ordered mesoporous alumina (OMA) thin films with systematically tailored pores has been an area of interest to many researchers.<sup>2,5,9–14</sup> In the soft-template method, the micellar assembly and pore architecture depend upon several factors such as the nature of surfactant, alumina precursor, and acid used along with a subtle tuning of their relative concentrations.<sup>2,5,9–14</sup> In the case of ordered mesoporous silica, control over pore architecture and mesopore symmetries has been achieved by using additives such as swelling agents,<sup>15</sup> cosolvents such as butanol,<sup>16</sup> cosurfactants,<sup>17</sup> inorganic salts,<sup>18</sup> tuning of some organic bridging groups in silica precursors,<sup>19</sup> and even presynthesized sol having  $SiO_2$  nanoparticles of different sizes.<sup>20–22</sup> However, reports on mesophase transition leading to generation of mesopores with tunable symmetries in an alumina system are very few. Recently we reported the synthesis of cubic ( $I\bar{m}\bar{3}m$ )<sup>5</sup> and hexagonal ( $P6mm$ )<sup>2</sup> mesoporous alumina films using F127 and P123 surfactants,

respectively, and a freshly prepared partially acetylacetone (acac) chelated aluminum secondary butoxide (ASB) (ASB/acac = 1:0.5) as the alumina precursor in the presence of  $HNO_3$ . It is noteworthy here that a long-standing problem known to sol-gel research is the instability of the alkoxide precursors. Different studies used different techniques to control the hydrolysis of alkoxides.<sup>23–25</sup> We have used partial acac chelated ASB to control its hydrolysis rate. Although the modified precursor apparently looks stable and clear over a month in alcohol solutions, it actually undergoes slow oligomerization reactions with respect to time. As a result, we observed different micellar structures in the presence of P123 when a differently aged precursor is used. So, by tuning the aging time of partially acac chelated ASB, different alumina sols were prepared to obtain different mesostructured alumina coatings. Recently, Wan et al.<sup>26</sup> showed the importance of aging of the surfactant–alumina composite mixture to obtain a 2D hexagonal ( $P6mm$ ) to face-centered cubic ( $Fm\bar{3}m$ ) mesophase in the presence of  $NH_3$  as a hydrolyzing agent. However, synthesis of thermally stable, ordered  $Ia3d$  and onion-like mesopores in alumina films have not yet been realized. In this context, it is worth mentioning that among the 3D mesoporous materials (such as  $Pm\bar{3}m$ ,  $I\bar{m}\bar{3}m$ ,  $Fm\bar{3}m$ , and  $Ia3d$ ), mesopores

Received: August 22, 2014

Revised: December 4, 2014

with  $Ia3d$  symmetry possess larger pore sizes and greater pore volumes.<sup>16,27–29</sup> The  $Ia3d$  mesoporous silica are shown to be good hosts for biomolecules<sup>27</sup> and are catalytically more active.<sup>28</sup> Stable onion-like mesostructured materials are expected to act as efficient hosts. For instance, Jun et al.<sup>30</sup> demonstrated that onion-like mesoporous silica can be used as a very good host for enzyme immobilization, and the greater curvature of such mesopores inhibits the leaching of enzymes.

We have already reported that the symmetry of mesopores could be easily tuned by merely changing the nature of surfactant from P123 to F127 (under the same synthetic conditions) owing to the differing size of the surfactants.<sup>2,5</sup> In our previous work we synthesized 2D hexagonal ( $P6mm$ ) mesoporous alumina film using a freshly prepared MAP in the presence of P123; the sol contained high molar ratios of MAP/ $HNO_3$  (1:1.72) and MAP/EtOH (1:55.13).<sup>2</sup> In this work, we report the effect of aging of the alumina precursor (MAP) solution upon the micellar transformation in the presence of a nonionic surfactant, P123, in relatively low acidic conditions (molar ratio of MAP/ $HNO_3$  = 1:0.67). Herein, the acid content with respect to ASB has been decreased intentionally to reduce the hydrolysis-condensation rates of the alumina precursor in the sol and to guide the formation of cubic mesopores using P123 surfactant.<sup>31,32</sup> P123 has been reported to preferentially generate hexagonal mesopores while F127 generally forms cubic mesostructures.<sup>2,5,33</sup> However, in the present work we could successfully synthesize alumina films with phase pure ordered  $Im\bar{3}m$ ,  $Ia3d$ , and onion-shaped mesopores separately by simply changing the aging time of the alumina precursor in the presence of P123 surfactant. An explanation for such a transformation has been proposed using transmission SAXS studies of sols and the FTIR of the alumina precursors. It is noteworthy that we could successfully synthesize three ordered phases from a single composition. To the best of our knowledge, synthesis of  $Ia3d$  and stable onion-like mesoporous alumina films is new.

## 2. EXPERIMENTAL SECTION

**2.1. Materials.** Mili-Q (Millipore) water (18.2 MΩ) was used throughout the study. All the chemicals were used without further treatment or purification. As certified by the company, 0.1–0.2 wt % of water was present in 1-propanol and 2-butanol.

**2.2. Preparation of Alumina Precursor Solution.** We have prepared the alumina precursor solution using ASB (Merck) and acetylacetone ( $\geq 98\%$ , Merck; abbreviated as acac) such that the molar ratio of ASB/acac is equal to 1:0.5.<sup>2,5</sup> Briefly, the required amount of ASB was rapidly transferred to the solvent mixture composed of 1-propanol (99.5%, Rankem; abbreviated as Pr<sup>OH</sup>), 2-butanol (99.5%, S.D. Fine-Chem Limited; abbreviated as Bu<sup>OH</sup>), and acac in a molar ratio of 1:0.54:0.12. The components were stirred in a sealed container for about an hour at room temperature ( $25 \pm 1^\circ C$ ) to obtain a partially chelated ASB–acac alumina precursor solution. To prepare 20 g of alumina precursor, 7 g of ASB were mixed with 13 g of the solvent–acac mixture. The solvent–acac mixture (13 g) contained a maximum of  $\sim 0.023$  g of water, and thus, ASB/H<sub>2</sub>O is 1:0.045. Since ASB is very reactive toward water, it would react with all the water as soon as they are mixed. This alumina precursor solution was used at different stages of aging (at  $25 \pm 1^\circ C$ ) for the synthesis of sols and ordered mesoporous alumina films. The modified alumina precursor shall be designated as MAP<sub>x,d</sub>, where ‘x’ represents the number of days of aging while ‘MAP’ and ‘d’ stand for ‘modified alumina precursor’ and ‘day’, respectively. For instance, MAP<sub>15d</sub> means the alumina precursor is used after 15 days of aging.

**2.3. Preparation of Ordered Mesoporous Alumina Films.** The synthesis of mesostructured alumina sol is similar to our previous

report, but in the present work the composition of the sol is different.<sup>2</sup> 1.6 g of Pluronic P123 ( $EO_{20}PO_{70}EO_{20}$ ,  $M_n = 5800$ , Sigma-Aldrich) and 8.0 g of ethanol (99.99%, Merck) were stirred for 2 h at room temperature ( $25 \pm 1^\circ C$ ) until complete dissolution of the surfactant. Then 1 g of  $HNO_3$  (70 wt %, S. D. fine-chem limited) was added and stirred for 5–10 min followed by addition of 11.66 g of the alumina precursor (MAP<sub>x,d</sub>). The stirring was continued for 5 h to obtain homogeneous alumina sol. The molar ratio of ASB/acac/P123/EtOH/ $HNO_3$  in the resultant sol was 1:0.5:0.017:10.4:0.67. It is to be noted that, during the synthesis, water was not added externally but the total water content in the sol (molar ratio of ASB/H<sub>2</sub>O  $\approx 1:1$ ) comes from the  $HNO_3$  used during the synthesis. Dip-coated films were prepared on glass substrates using Dip-Master 200 (Chemate Corporation, USA; withdrawal velocity of 8 in. min<sup>-1</sup>) under ambient condition ( $25 \pm 1^\circ C$  and 55–60% relative humidity). The films were dried for 16 h at 60 °C, followed by heating at 500 °C in air (ramp: 1 °C min<sup>-1</sup>) with a holding time of 2 h to eliminate all the organics.<sup>2</sup> Mesostructured alumina sols prepared from MAP<sub>x,d</sub> shall be designated as OMAS<sub>x,d</sub> and the corresponding dip-coated ordered mesoporous alumina film will be abbreviated as OMAF<sub>x,d</sub>. It is to be noted that the alumina sols and films showing prominent mesophase transformations and different phase pure mesopores shall be discussed in detail. We prepared sols and coatings with  $x = 0, 10, 15, 20$ , and 30 but the mesophase symmetry of films with  $x = 0$  and 15 were similar to that of  $x = 10$  and 20, respectively; hence as representative examples, the detailed characterizations of MAP<sub>x,d</sub>, OMAS<sub>x,d</sub>, and OMAF<sub>x,d</sub> with  $x = 0, 15$ , and 30 have been presented in this work.

**2.4. Characterizations.** Attenuated total reflectance (ATR)–Fourier transformed infrared (FTIR) absorption spectra of the solutions were recorded by an Alpha FTIR spectrometer (Bruker, Germany) by placing a drop of the alumina precursors, MAP<sub>0d</sub>, MAP<sub>15d</sub>, and MAP<sub>30d</sub> on the clean ZnSe crystal surface. The raw small-angle X-ray scattering (SAXS) profiles of the alumina sols were recorded at  $20 \pm 2^\circ C$  in transmission mode using a Rigaku SmartLab X-ray diffractometer (9 kW; source Cu K $\alpha$  with  $\lambda = 1.5406$  Å). The sols were placed in borosilicate capillary tubes with an  $\sim 1.5$  mm diameter, and the capillaries were mounted at a fixed position on a capillary sample holder. Simulations and size distributions were evaluated through NANO-Solver software of Rigaku. Prior to data fittings, the raw SAXS profiles of mesostructured alumina sols ( $x = 0, 15$ , and 30) were corrected for background absorption and air scattering. SAXS profiles of the alumina precursors (MAP<sub>x,d</sub>;  $x = 0, 15$ , and 30) were also collected for subtraction purposes. The contributions from the respective alumina precursors have been subtracted from the corresponding raw SAXS profiles of OMAS sols to obtain corrected SAXS profiles for micellar size evaluation. Micellar size distributions were obtained from simulated fittings of the corrected SAXS profiles using “sphere” and “core–shell” models. Low and high angle X-ray diffraction (XRD) studies of ordered mesoporous alumina films (OMAF<sub>0d</sub>, OMAF<sub>15d</sub>, and OMAF<sub>30d</sub>) were carried out using the same diffractometer. The observed low angle XRD patterns were deconvoluted through the MDI JADE 7 software of Rigaku to obtain the expected well-resolved peaks.<sup>34</sup> The best-fitted patterns in the fwhm (full width at half maxima) mode have been considered in each case. Refractive index and thickness measurements of the OMAF<sub>x,d</sub> films (coated on single-side polished Si wafer) were carried out using a J.A. Woolam Co. M 2000 spectroscopic ellipsometer. All the refractive indexes have been reported at the wavelength of 633 nm.<sup>2,5</sup> Field emission scanning electron microscopic (SEM) analysis and elemental area mappings (energy dispersive X-ray spectra, EDS) of the calcined OMAF<sub>x,d</sub> films were carried using a Carl Zeiss, Supra-35VP (Germany) instrument. Transmission electron microscopy (TEM) images of these film samples were acquired from Tecnai G<sup>2</sup> 30ST (FEI) operating at 300 kV by placing trace amounts of scratched off film samples on carbon coated Cu TEM grids.

## 3. RESULTS AND DISCUSSION

It is well-known that aluminum alkoxides tend to form polymeric alkoxide species on standing for long time. This

phenomenon (called oligomerization) takes place via donation of lone pairs of electrons from the alkoxy groups of other aluminum alkoxides molecules. In case of ASB partially chelated with acac (i.e. MAP) this oligomerization process occurs relatively slowly. We performed solution phase ATR-FTIR of MAP (Figure 1) to confirm the occurrence of such

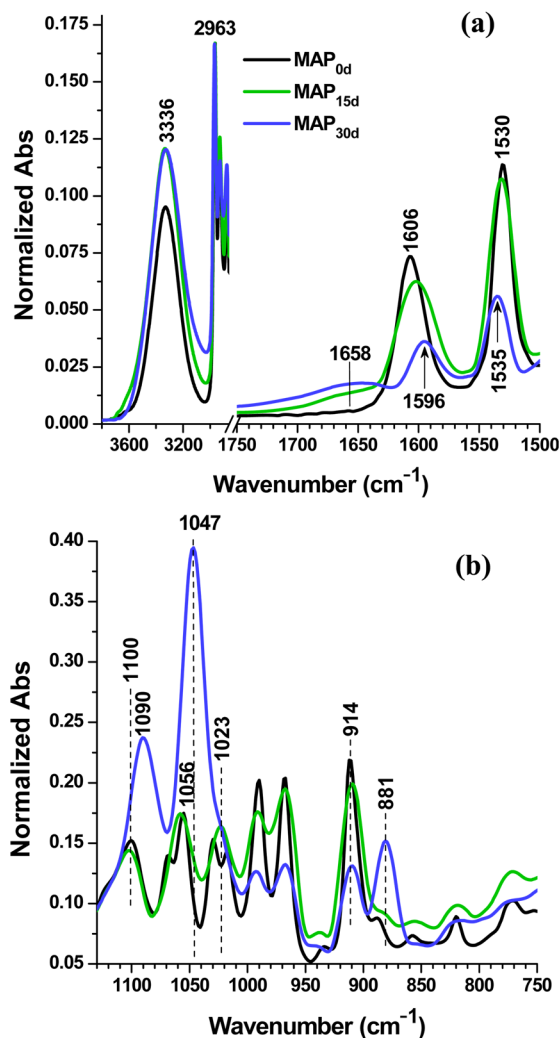


**Figure 1.** FTIR spectra of MAP<sub>0d</sub>, MAP<sub>15d</sub>, and MAP<sub>30d</sub> showing (a) the changes in acac bonding with Al of the alumina precursor and (b) the formation of b-OBu<sup>s</sup> bonding with aging of the sol at the expense of t-OBu<sup>s</sup> groups due to self-association of the alumina units. All spectra were normalized with respect to the C–H stretching intensity at 2963 cm<sup>-1</sup>.

oligomerization in the MAP with time. For the purpose of comparison, ATR-FTIR spectra of all MAP solutions (Figure 1) have been normalized with respect to the C–H stretching at 2963 cm<sup>-1</sup> considering the concentration of this species remain same and the intensity of this peak will not be affected much during aging. It must be noted that the initial traces water (present in the Bu<sup>s</sup>OH/Pr<sup>n</sup>OH; see section 2.2) reacts with very small amount of ASB, and thus the remaining MAP<sub>0d</sub> solution should be considered as water-free. Therefore, the peak at 3336 cm<sup>-1</sup> ( $\nu_{O-H}$ ) shown in Figure 1a appears mainly due to the presence of alcoholic OH. The FTIR spectrum of free acac liquid shows a weak doublet near 1706 and 1729 cm<sup>-1</sup> (corresponds to ketonic C=O) and a strong band at ~1606

cm<sup>-1</sup> due to enolic C=O (see the ATR-FTIR spectrum of liquid acac in Figure S1, Supporting Information). According to Tayyari et al.<sup>33</sup> this strong band is actually the superposition of  $\nu_{C-C}$  (1625 cm<sup>-1</sup>) and  $\nu_{C-O}$  (1600 cm<sup>-1</sup>) modes. Owing to chelation in MAP<sub>0d</sub> we observe two prominent peaks at 1606 and 1530 cm<sup>-1</sup> assignable to  $\nu_{C-C}$  coupled with  $\nu_{C-O}$  (represented as  $\nu_{C-C+C-O}$ ) and  $\nu_{C-O}$  coupled with  $\nu_{C-C}$  (represented as  $\nu_{C-O+C-C}$ ), respectively.<sup>2,35,36</sup> The FTIR spectrum of MAP<sub>30d</sub> shows a prominent shift in these peaks to 1596 and 1535 cm<sup>-1</sup>, respectively. Apart from this, a broad but prominent hump with maxima near ~1658 cm<sup>-1</sup> in MAP<sub>30d</sub> indicates the presence of acac with more C=O and C=C characteristics. For better understanding we have also recorded the ATR-FTIR of pure ASB, acac, Bu<sup>s</sup>OH and Pr<sup>n</sup>OH liquids (see Supporting Information, Figure S1). The peaks of ASB at ~1101, 988, and 914 cm<sup>-1</sup> are related to the C–O stretching mode of terminal sec-butoxy (t-OBu<sup>s</sup>) groups attached to Al (Figure S1a).<sup>37</sup> FTIR of the freshly prepared alumina precursor (MAP<sub>0d</sub>) shows the distinguishable peaks characteristic of t-OBu<sup>s</sup> at 1100 and 914 cm<sup>-1</sup> (Figure 1b and Figure S1a). The appearance of doublet peaks near 1069, 1055 cm<sup>-1</sup>, and 1029, 1017 cm<sup>-1</sup> is due to the presence of solvent Pr<sup>n</sup>OH (Figure 1b; also see Figure S1a for comparison). Upon aging of the MAP for 15 days, the peaks in the region 1100–800 cm<sup>-1</sup> broadens (Figure 1b). The doublet peaks observed in the case of MAP<sub>0d</sub> merges into two broad peaks at 1057 and 1023 cm<sup>-1</sup>, respectively, and the intensity of the peaks corresponding to t-OBu<sup>s</sup> linked to Al decreases. It is noteworthy here that the shifting in the peak positions and intensities are more prominent in MAP<sub>30d</sub>. We observe very strong peaks at 1047 and 881 cm<sup>-1</sup> which are due to the presence of bridging alkoxy groups (b-OBu<sup>s</sup>) associated with Al.<sup>37</sup> It can be noted here that the extremely strong peak at 1047 cm<sup>-1</sup> has a small contribution from the Pr<sup>n</sup>OH also. A concomitant decrease in intensity of the peak at 914 cm<sup>-1</sup> and appearance of a peak at 881 cm<sup>-1</sup> suggest that the frequency of t-OBu<sup>s</sup> decreases due to the formation of more bridged bonds (b-OBu<sup>s</sup>; Figure 1b). The O atoms of the t-OBu<sup>s</sup> linked to alumina species (of MAP) act as a nucleophile and attack the partially electropositive Al atom<sup>23,24,38</sup> thereby causing formation of an oligomer. It is to be noted that we are not considering the actual structure of the MAP species to avoid complexity. However, the FTIR studies confirm the oligomerization of alumina with aging. Therefore, the chemical nature of apparently similar MAP solutions (from different aging times) changes due to slow molecular association leading to the formation of oligomers to different degrees. This is expected to induce differences in the micellar behavior of P123 in OMAs.

The mesophase transformations in silica systems have been related to a change in the micellar dimensions.<sup>18,39</sup> Small angle X-ray scattering (SAXS) is a very interesting nondestructive tool for studying the dynamics of the micelles and their behavior in the presence of other entities in the solution. It is well-known that dense or bigger particles efficiently scatter the X-rays; i.e., X-rays diffuse scattering occurs owing to the differences in the electron densities. The angle of X-rays scattering is inversely related to the scattering region. According to Born approximation, the scattering amplitude,  $A(q)$ , is expressed as

$$A(q) = \int_v \Delta\rho(r)e^{iqr} dr \quad (1)$$

$$q = (4\pi/\lambda) \cdot \sin \theta \quad (2)$$

where  $q$  is the scattering vector,  $v$  is the target volume for the integral over the entire medium,  $\Delta\rho$  is the electron density difference, and  $\lambda$  is the wavelength of the X-ray.

The scattering intensity,  $I(q)$ , is given by

$$I(q) = A(q) \cdot A^*(q) \quad (3)$$

If the particles, whose scattering is considered, possess a definite shape, then  $I(q)$  is expressed in terms of the structure factor,  $S(q)$ , and the form factor,  $F(q)$ , as

$$I(q) = |F(q)|^2 S(q) \quad (4)$$

$F(q)$  is dependent upon the shape of the particle in consideration while  $S(q)$  considers the interparticle distance and order of the particle arrangement. Usually in dilute solutions the particles are randomly distributed in the medium and  $S(q)$  becomes unity.<sup>18,40,41</sup> Each P123 molecule consists of a couple of more hydrophilic PEO (polyethylene oxide) units and a chain of comparatively less hydrophilic PPO (polypropylene oxide) units. In the presence of a polar solvent (such as alcohol), the PEO units interact with the solvent and assemble in the outer part of the micelles while the PPO units remain in the core.<sup>2</sup> The small contributions from monomeric P123 molecules may be neglected during the SAXS evaluations.<sup>40–42</sup> It is assumed that the core contains the PPO units only while the shell mainly contains solvated PEO (i.e. PEO + alcoholic solvent). The alumina units (from MAP) attach themselves to the shell of the micelle forming a P123/alumina composite in the OMAS sol. With aging, oligomerization of MAP takes place and the size of MAP is expected to change. Therefore, to have a less complex environment the scattering contribution from the corresponding  $\text{MAP}_{\text{xd}}$  (background contribution) has been removed from the overall scattering pattern of the OMAS<sub>xd</sub>.<sup>39</sup> Henceforth, for data fittings we shall consider the corrected intensity,  $I(q)$ , which is expressed as

$$I(q) = I(q') - I(q^\circ) \quad (5)$$

where  $I(q')$  and  $I(q^\circ)$  are the scattering intensities of OMAS<sub>xd</sub> and the corresponding  $\text{MAP}_{\text{xd}}$ , respectively. Therefore, each micelle is considered as an individual particle, and being in dilute solution, it is expected that the value of  $S(q)$  is equal to 1.

In solution, micelles may be either spherical or cylindrical, and the development of ordered material with a particular symmetry depends upon the size and shape of these micelles. Therefore, we used both the ‘sphere’ and the ‘core–shell’ models for fitting the corrected SAXS profiles. The ‘form factor’ for spherical and core–shell particles with a radius ‘ $R$ ’ is expressed as

$$[F(q, R)]^{\text{sphere}} = (\rho_1 - \rho_o) \cdot (4\pi/q^3) \{ \sin(qR) - qR \cos(qR) \} \quad (6)$$

$$[F(q, R)]^{\text{core-shell}} = (\rho_{\text{core}} - \rho_{\text{shell}}) \cdot (4\pi/q^3) \{ \sin(qR) - qR \cos(qR) \} + (\rho_o - \rho_{\text{core}}) \cdot (4\pi/q^3) \{ \sin q(R+d) - q(R+d) \cos q(R+d) \} \quad (7)$$

where  $\rho_1$ ,  $\rho_{\text{core}}$ ,  $\rho_{\text{shell}}$ , and  $\rho_o$  are the densities of particle (P123), core (PPO), shell (PEO), and the solvent, respectively and  $R$

represents the radius of the core and  $d$  is the thickness of shell of the micelle. The densities of P123, PPO core, PEO shell, and solvent (ethanol) are 1.04, 1.01, 1.2, and 0.8 g cm<sup>-3</sup> respectively.<sup>42</sup> As we have already considered the MAP solutions as background, the density from other liquids has not been considered.

The close proximity between the raw and simulated profiles with a low residual value ( $R$ -factor) is essential for error-free evaluation of data. Better data fittings were obtained using the ‘core–shell’ model (Figure 2) in comparison to the ‘sphere’ model (see Supporting Information, Figure S2). This is consistent with the other reports where micelles have been best described by the ‘core–shell’ model in which the core and shell possess relatively different densities.<sup>40–44</sup> Also, the ‘core–shell’ model can be applied to both spherical and cylindrical micelles. Therefore, in this present case, we shall discuss the

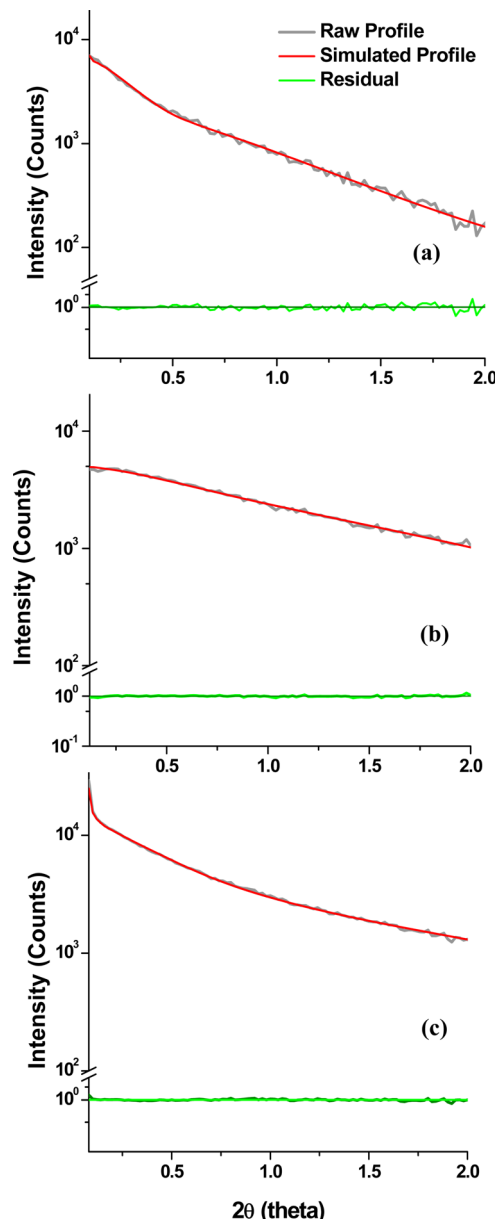


**Figure 2.** Corrected SAXS profiles of P123 micelles in (a) OMAS<sub>0d</sub>, (b) OMAS<sub>15d</sub>, and (c) OMAS<sub>30d</sub> sols fitted with ‘core–shell’ model (NANO Solver program of Rigaku Corporation).

detailed results obtained from the core–shell data analysis only. Table 1 represents the numerical values obtained from the

**Table 1.** Average Micellar Size ( $D_m$ ), Core Size ( $D_c$ ), and Normalized Dispersion ( $\sigma$ ) of P123 Micelle in OMAS<sub>xd</sub> Sols Have Been Evaluated from SAXS Fittings Using ‘Core–Shell’ Model, with the Residual Value (R-Factor) Also Tabulated

Sol	$D_m$ (nm)	$\sigma$ (%)	$D_c$ (nm)	R-factor
OMAS <sub>0d</sub>	3.8	49.4	1.9	1.19
OMAS <sub>15d</sub>	5.5	57	2.9	0.44
OMAS <sub>30d</sub>	8.3	57	5.7	0.36

profile fittings given in Figure 2. The average size of P123 micelles increases from 3.8 nm (OMAS<sub>0d</sub>) to 8.3 nm for OMAS<sub>30d</sub>. It is also evident that there is an increase in the size of the core from 1.9 to 5.7 nm with increasing aging time of the precursor. The micellar size distribution curves, shown in Figure 3, represent the variation in the size of the P123 micelle.

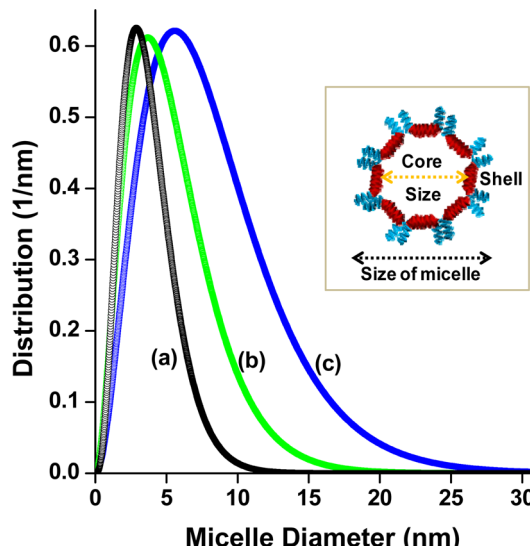


**Figure 3.** Size distribution of P123 micelle in (a) OMAS<sub>0d</sub>, (b) OMAS<sub>15d</sub>, and (c) OMAS<sub>30d</sub>. The schematic representation of a micelle with core–shell structure is shown in the inset.

It is to be noted that the nature of the size distribution curve depends upon the normalized dispersion ( $\sigma$ ). Mathematically,  $\sigma$  is defined as the standard deviation in the size of particles normalized by the average size:

$$\sigma = \frac{\sqrt{\langle \delta R^2 \rangle}}{R_0} \quad (8)$$

For instance, the distribution curves for OMAS<sub>15d</sub> and OMAS<sub>30d</sub> become broader (with greater  $\sigma$  value) compared to OMAS<sub>0d</sub>; this hints at the elongation of the micelles with time.<sup>42–44</sup> A schematic representation of the P123 micellar “core–shell” model is shown in the inset of Figure 3.

In the presence of HNO<sub>3</sub>, controlled hydrolysis–condensation of the alumina precursor (in OMAS) forms extensive Al–O–Al linkages. The dip-coated films prepared from the OMAS<sub>xd</sub> sols were dried, and calcinations of the mesostructured films at 500 °C result in the removal of the organic groups leading to the formation of mesoporous alumina. The

volume percent porosity of the films ( $P_{\%}$ ) have been evaluated from the refractive index values using the Lorentz–Lorentz equation (see Supporting Information, Table S1).<sup>2,5</sup> OMAF<sub>15d</sub> has the highest  $P_{\%}$  value (51%) in comparison to the other two films, OMAS<sub>0d</sub> (44%) and OMAS<sub>15d</sub> (48%). Such a trend in the  $P_{\%}$  has been explained later after a thorough introspection into the overall mesostructure of the films. The observed increase in the average thicknesses of the films is related to the use of differently aged alumina precursors (MAP<sub>xd</sub>) with different degrees of oligomerization. Greater oligomerization results in more cross-linked Al–O–Al units, and the overall thickness of the films increases.<sup>45</sup>

Digital photographs of OMAF<sub>0d</sub>, OMAF<sub>15d</sub>, and OMAF<sub>30d</sub> films and their SEM images are shown in Figure S3 (Supporting Information). The macroscopic photos reveal the transparent nature of the films, while crack-free homogeneous film surfaces can be observed from the low resolution SEM images. The corresponding selected area mappings (using the SEM-EDS) confirmed the presence of uniformly distributed Al in the entire matrix.

Based upon the SAXS results it is expected that a change in the micellar size would induce a change in the ordered arrangements of the mesopores after removal of P123. We performed low angle XRD of the corresponding calcined films. Figure 4 shows the XRD patterns (represented as deep green lines) for each of the samples along with their corresponding deconvoluted patterns (represented as blue lines; see section 2.4) for a better understanding of the symmetry assignments.<sup>34</sup> The original XRD pattern of OMAF<sub>0d</sub> reveals two prominent peaks at 0.62° and 1.10° and a small hump at 0.88° (see Figure 4a). After deconvolution (see the blue curve in Figure 4a) we observe three distinct peaks at 0.62°, 0.87°, and 1.11° assignable to (110), (200), and (211) planes of  $Im\bar{3}m$  symmetry, respectively. It is to be noted that such an assignment of symmetry has been made as the peak positions are in the ratio  $1:\sqrt{2}:\sqrt{3}$ , characteristic of  $Im\bar{3}m$  symmetry.<sup>5,33,46</sup> Similarly, in the case of OMAF<sub>15d</sub> the original spectrum shows two prominent peaks (Figure 4b) which can be resolved into three peaks at 0.74°, 0.9°, and 1.15° maintaining the ratio  $\sqrt{3}:\sqrt{4}:\sqrt{7}$ . Thus, these peaks are assignable to the (211), (220), and (321) planes of the  $Ia3d$  space group, respectively.<sup>16,33,46</sup> OMAF<sub>30d</sub> reveals two main peaks at 0.63° and 0.95° due to the (200) and (300) of the lamellar structure, respectively. The corresponding deconvoluted curve shows a distinct shoulder at 1.24° which can be assigned for the (400) plane. The appearance of these peaks indicates that the mesoporous lamellar alumina is stable.<sup>15,47</sup> The presence of the lamellar phase is further clarified with the help of the TEM images of the OMAF<sub>30d</sub> sample.

TEM studies on the film samples supported the XRD results. The images of the mesoporous samples were distinguishably different in the three cases. Figure 5a shows the bright field TEM image of OMAF<sub>0d</sub> with  $Im\bar{3}m$  symmetry. It shows clear cubic structure with a neighboring pore-to-pore distance of 13.7 nm (see the pores marked with circles in Figure 5b; the corresponding model is shown in the upper inset of Figure 5a). This matches with the (110) peak position in the low angle XRD pattern of OMAF<sub>0d</sub> (Figure 4a). The energy dispersive X-ray spectra (EDS) of the OMAF<sub>0d</sub> shown in the lower inset of Figure 5a, revealed the presence of Al and O (from the sample) along with the small signals of C and Cu (from the C-coated Cu grid). The diffused nature of the selected area electron diffraction (SAED) pattern of the sample is consistent with

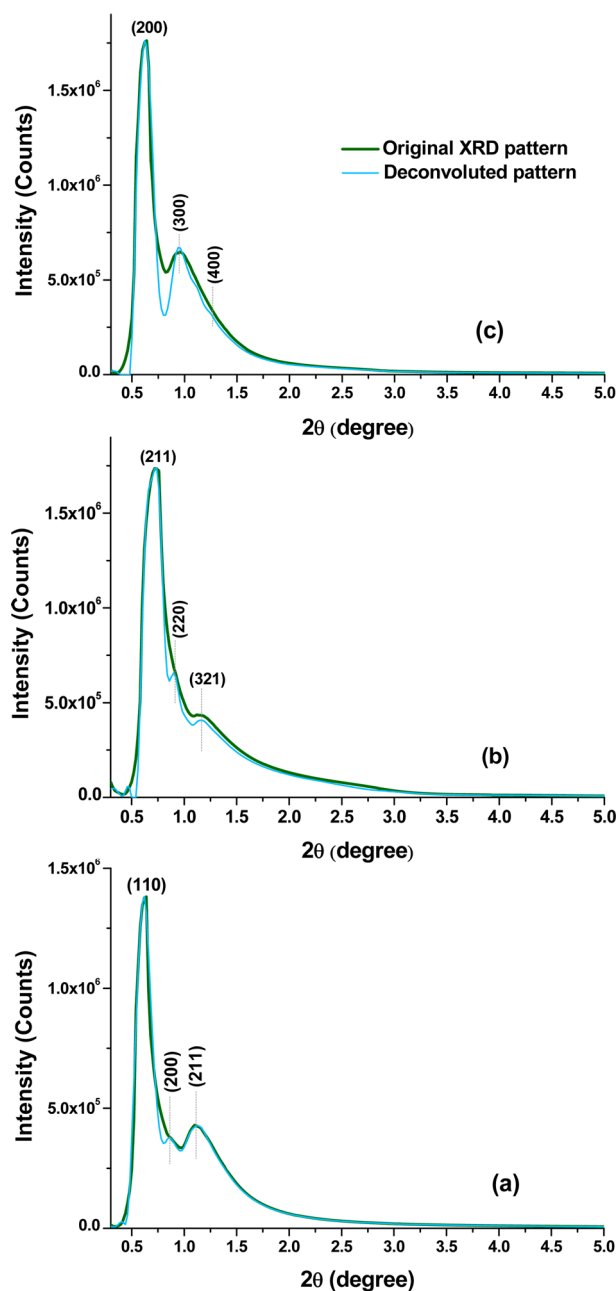


**Figure 4.** Low angle XRD patterns of the calcined (a) OMAF<sub>0d</sub>, (b) OMAF<sub>15d</sub>, and (c) OMAF<sub>30d</sub> films.

the corresponding high angle XRD profile (see Figure S4, Supporting Information) which confirms the amorphous nature of the samples.<sup>2,5</sup> TEM images of the OMAF<sub>15d</sub> sample is presented in Figure 5c. A magnified portion from Figure 5c shows the ‘wagon wheel-like’ pattern of the mesopores (see Figure 5d and the corresponding model in the upper inset of Figure 5c) similar to the TEM images reported for cubic *Ia3d* mesoporous silicas.<sup>16,48</sup> The neighboring pore-to-pore distance obtained from the magnified TEM image (see Figure 5c) is 11.9 nm; this corresponds to the (211) peak position as observed in the low angle XRD pattern (Figure 4b). We observed onion-like mesopores in the OMAF<sub>30d</sub> sample (Figure 6). These mesopores are lamellar in nature, as the low angle XRD pattern of OMAF<sub>30d</sub> showed (200), (300), and (400) peaks with a ratio of 2:3:4. Although onion-like mesoporous

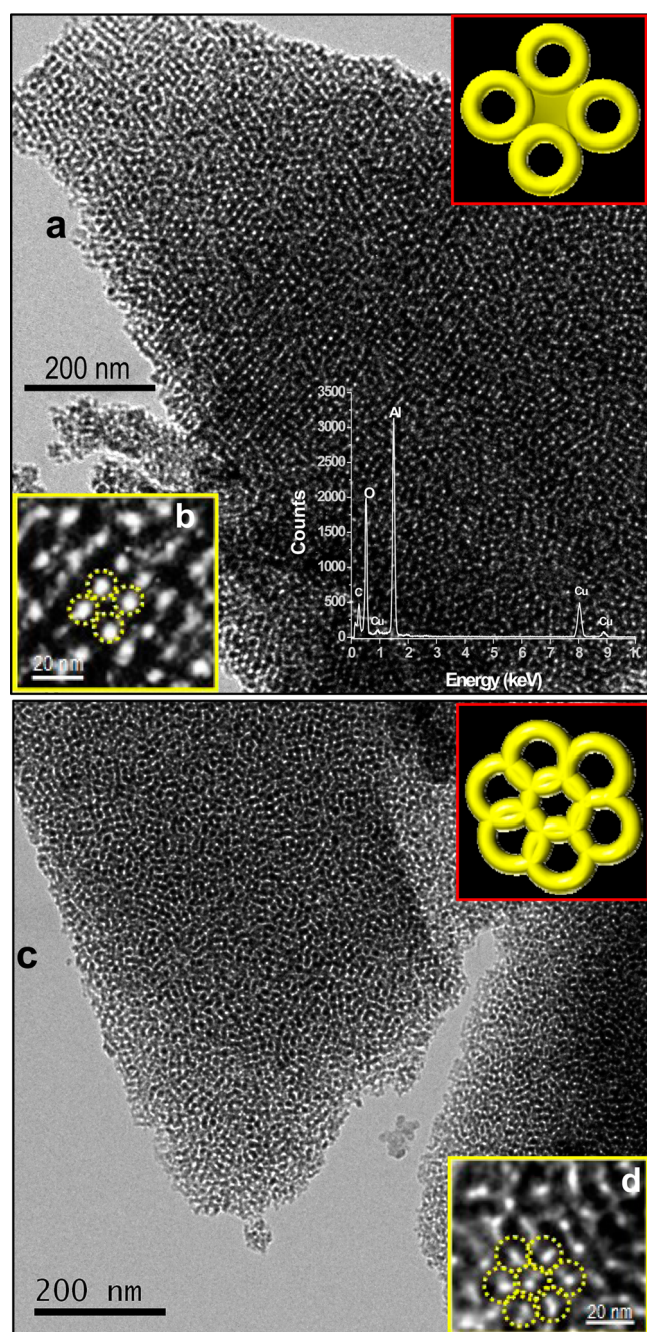


**Figure 5.** TEM images of the calcined (a, b) OMAF<sub>0d</sub> and (c, d) OMAF<sub>15d</sub> samples showing *Im*<sup>3</sup>*m* and *Ia*<sup>3</sup>*d* mesopores, respectively. The energy dispersive X-ray spectrum (EDS) is shown in lower inset of (a). The upper insets in (a) and (c) represent the models showing orientation of mesopores in accordance with the corresponding magnified TEM images.

silica has been reported earlier, this type of mesopores in the alumina system has been successfully synthesized for the first time. The highest volume porosity (see Table S1) in OMAF<sub>15d</sub> can now be related to its cubic *Ia3d* mesostructure; this is found to be consistent with the reports of Vinu et al.<sup>27,29</sup>

Scheme 1 shows the mechanism of mesophase transformation in the dried OMAF<sub>xd</sub> owing to the presence of different sized P123 micelles in the corresponding OMAs<sub>xd</sub>. To understand the role of aging in guiding the final symmetry of mesopores we have varied only the aging time of MAP, keeping

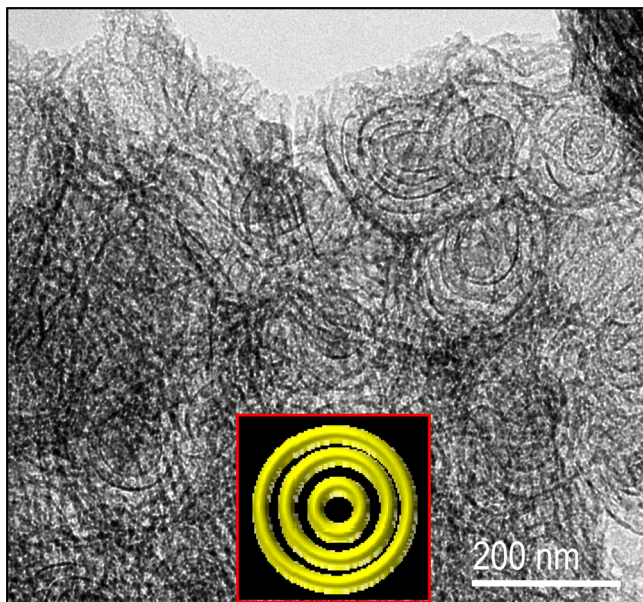
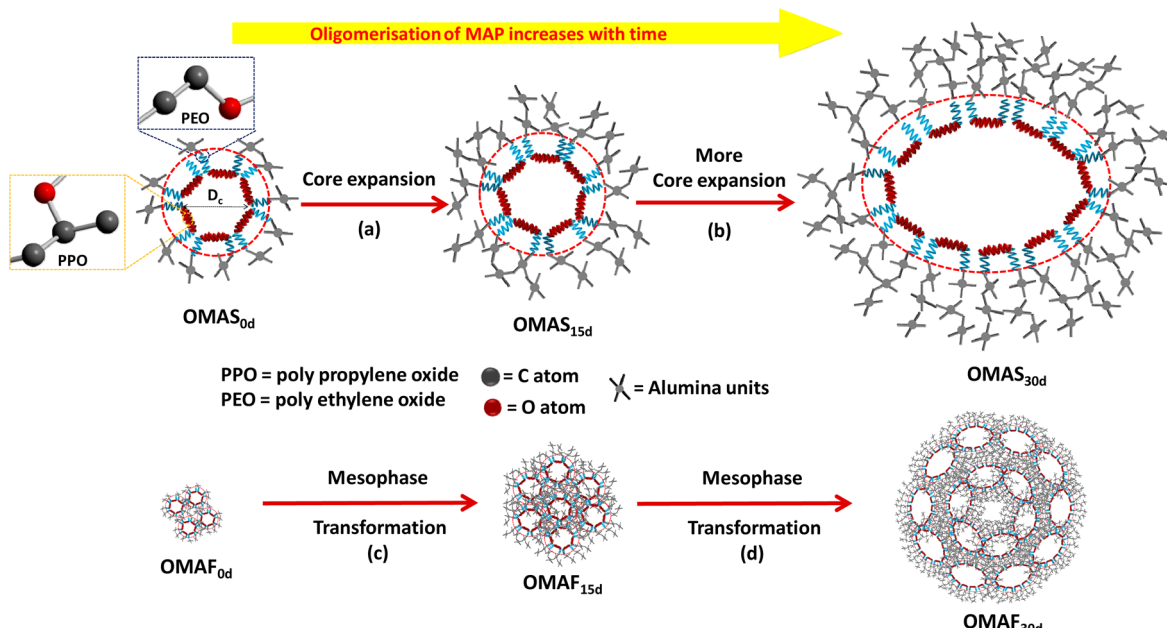


**Figure 6.** TEM image of the heat-treated OMAF<sub>30d</sub> sample with *onion-like* mesopores. The inset showing the model of *onion-like* mesopore.

all the other parameters the same. Tolbert et al. reported that more cross-links or oligomerization in the case of silica precursors leads to mesophase transformation from  $P6mm$  to lamellar via an intermediate  $Ia3d$  stage.<sup>49</sup> Bollmann et al. investigated the role of aging of the surfactant/silica sol in guiding the mesophase transformation of nanoporous silica from rhombohedral ( $R3m$ ) to 2D rectangular ( $c2m$ ) to double-gyroid (distorted  $Ia3d$ ) and finally to lamellar. They related

such transformations to the decrease in the interfacial curvature between the hydrophilic and hydrophobic parts of the surfactant due to the decrease in interaction between the EO (of surfactant) and silica in the less hydrophilic larger silica oligomers.<sup>21,22</sup> In our case too, oligomerization of the alumina precursor takes place with time and consequently greater cross-linked alumina precursor is generated (see Scheme 1 a, b). Therefore, when an aged MAP is added to the alcoholic P123 solution, these cross-linked alumina precursors behave differently. A decrease in the hydrophilic character of highly bridged alkoxo groups in the case of aged MAP reduces their interaction with the hydrophilic part (PEO) of the P123 surfactant.<sup>22</sup> It is likely that more cross-linked MAP would be very rigid and should tend to form a mesostructure with lower curvature.<sup>32</sup> The larger alumina units in OMAS<sub>30d</sub> would interact with two PEO tails per P123 molecules (see Scheme 1 a and b). This creates a structural strain in outer PEO/alumina blocks resulting in an overall swelling of the core (PPO), especially in the OMAS<sub>30d</sub> (Figure 3 and Table 1). SAXS studies also suggest that the micelles in OMAS<sub>15d</sub> and OMAS<sub>30d</sub> are slightly elongated in nature. As the edges and corners of particles are usually very reactive, upon thermal treatment (at 500 °C) the comparatively elongated ends of the micelles (in OMAS<sub>30d</sub>) tend to merge together which explains the formation of *onion-like* mesopores. The observed transformation and SAXS results can also be correlated with the concept of a ‘packing parameter’. It is well-known that the shape and size of micelles play a pivotal role in governing the overall mesoscopic assembly. To qualitatively describe the micelle packing or assembly, the term ‘surfactant packing parameter’, designated as ‘g’, is often used. The surfactant packing parameter ( $g$ ) is directly proportional to the ratio between the effective volume of the hydrophobic group and that of the hydrophilic group.<sup>17</sup>

**Scheme 1.** (a, b) Gradual Increase in the PPO Core in OMAS<sub>xd</sub> Sols ( $x = 0, 15$ , and  $30$ ). (c, d) Mesophase Transformations in the OMAF<sub>xd</sub> Films through Evaporation Induced Self Assembly (EISA) of the P123/Alumina Composites upon Drying at 60 °C<sup>a</sup>



<sup>a</sup>The P123 micelles are enclosed in red dotted circles for visual clarity. Different sizes of the alumina units (attached to the PEO shell) represent different extents of oligomerization in MAP with time. The bond lengths and bond angles of PPO, PEO, and alumina units drawn in the scheme are arbitrary.

The values of 'g' follow the order  $I\bar{m}3m < Ia3d <$  lamellar; i.e., a mesophase with lower curvature will have a higher value of g. In this case too, as the size of the hydrophobic core increases the value of g will also increase resulting in the formation of a mesostructure with lower curvature. Thus, the mesophase transformation can be connected to the different structures of the aged alumina precursors and their interaction with P123. As a result, freshly prepared MAP<sub>0d</sub> yielded cubic  $I\bar{m}3m$  pores with the smallest pore size, intermediate aged MAP<sub>15d</sub> generated larger pores with  $Ia3d$  symmetry, and more aged MAP<sub>30d</sub> produced continuous pores having an onion-like structure with the lowest curvature energy.<sup>50</sup>

## 4. CONCLUSION

We have shown structural transformation of an apparently stable partially acac chelated ASB solution with respect to time. This transformation has been successfully utilized to prepare sols in the presence of the structure directing agent, P123, and tunable mesostructured coatings. Transmission SAXS studies of sols clearly showed micellar transformations which, in turn, helped to obtain stable mesoporous alumina films having  $I\bar{m}3m$ ,  $Ia3d$ , and *onion-like* pore arrangements as confirmed by the low angle XRD and TEM studies. The formation of differently ordered mesoporous alumina films on glass is noteworthy which could find interesting applications in catalysis.

## ■ ASSOCIATED CONTENT

### Supporting Information

Refractive index and thickness results (Table S1); ATR-FTIR spectra (Figure S1); SAXS profile fittings using the "sphere" model (Figure S2); SEM and digital photographs of the OMAF<sub>xd</sub> films (Figure S3); TEM and high angle XRD of OMAF<sub>0d</sub> (Figure S4). This material is available free of charge via the Internet at <http://pubs.acs.org>.

## ■ AUTHOR INFORMATION

### Corresponding Author

\*Telephone: +91 33 23223403. Fax: +91 33 24730957.

### Notes

The authors declare no competing financial interest.

## ■ ACKNOWLEDGMENTS

A.M. thanks CSIR, India for providing a fellowship. Financial support from DST (Government of India) is thankfully acknowledged.

## ■ REFERENCES

- (1) Hu, W.; Zheng, F.; Hu, B. Simultaneous Separation and Speciation of Inorganic As(III)/As(V) and Cr(III)/Cr(VI) In Natural Waters Utilizing Capillary Microextraction On Ordered Mesoporous Al<sub>2</sub>O<sub>3</sub> Prior to Their On-Line Determination by ICP-MS. *J. Hazard. Mater.* **2008**, *151*, 58–64.
- (2) Mitra, A.; Jana, D.; De, G. Facile Synthesis of Hexagonally Ordered Mesoporous Aluminium Oxide Thin Films with High Catalytic Activity. *Microporous Mesoporous Mater.* **2012**, *158*, 187–194.
- (3) Márquez-Alvarez, C.; Žeilkova, N.; Perez-Pariente, J.; Čejka, J. Synthesis, Characterization and Catalytic Applications of Organized Mesoporous Aluminas. *Catal. Rev.-Sci. Eng.* **2008**, *50*, 222–286.
- (4) Oikawa, T.; Ookoshi, T.; Tanaka, T.; Yamamoto, T.; Onaka, M. A New Heterogeneous Olefin Metathesis Catalyst Composed Of Rhenium Oxide and Mesoporous Alumina. *Microporous Mesoporous Mater.* **2004**, *74*, 93–103.
- (5) Mitra, A.; Jana, D.; De, G. A Facile Synthesis of Cubic ( $I\bar{m}3m$ ) Alumina Films on Glass with Potential Catalytic Activity. *Chem. Commun.* **2012**, *48*, 3333–3335.
- (6) Morris, S. M.; Fulvio, P. F.; Jaroniec, M. Ordered Mesoporous Alumina-Supported Metal Oxides. *J. Am. Chem. Soc.* **2008**, *130*, 15210–15216.
- (7) Yuan, Q.; Yin, A. X.; Luo, C.; Sun, L. D.; Zhang, Y.-W.; Duan, W. T.; Liu, H. C.; Yan, C. H. Facile Synthesis For Ordered Mesoporous  $\gamma$ -Aluminas With High Thermal Stability. *J. Am. Chem. Soc.* **2008**, *130*, 3465–3472.
- (8) Dandapat, A.; Jana, D.; De, G. Synthesis of Thick Mesoporous  $\gamma$ -Alumina Films, Loading of Pt Nanoparticles, and Use of The Composite Film As A Reusable Catalyst. *ACS Appl. Mater. Interfaces* **2009**, *1*, 833–840.
- (9) Jiang, X.; Ishizumi, A.; Suzuki, N.; Naito, M.; Yamauchi, Y. Vertically-oriented Conjugated Polymer Arrays In Mesoporous Alumina Via Simple Drop-Casting and Appearance of Anisotropic Photoluminescence. *Chem. Commun.* **2012**, *48*, 549–551.
- (10) Mazaj, M.; Costacurta, S.; Logar, N. Z.; Mali, G.; Tušar, N. N.; Innocenzi, P.; Malfatti, L.; Thibault-Starzyk, F.; Amenitsch, H.; Kaučič, V.; Soler-Illia, G. J. A. A. Mesoporous Aluminophosphate Thin Films With Cubic Pore Arrangement. *Langmuir* **2008**, *24*, 6220–6225.
- (11) Oveisi, H.; Jiang, X.; Imura, M.; Nemoto, Y.; Sakamoto, N.; Yamauchi, Y. A Mesoporous  $\gamma$ -Alumina Film with Vertical Mesoporosity: The Unusual Conversion from a Mesostructure to Vertically Oriented  $\gamma$ -Alumina Nanowires. *Angew. Chem., Int. Ed.* **2011**, *50*, 7410–7413.
- (12) Gu, D.; Schüth, F. Synthesis of Non-Siliceous Mesoporous Oxides. *Chem. Soc. Rev.* **2014**, *43*, 313–344.
- (13) Pidot, L.; Grossi, D.; Soler-Illia, G. J. A. A.; Crepaldi, E. L.; Sanchez, C.; Albouy, P. A.; Amenitsch, H.; Euzend, P. Hexagonally Organised Mesoporous Aluminium–Oxo–Hydroxide Thin Films Prepared by the Template Approach. In Situ Study of the Structural Formation. *J. Mater. Chem.* **2002**, *12*, 557–564.
- (14) Kuemmel, M.; Grossi, D.; Boissière, C.; Smarsly, B.; Brezesinski, T.; Albouy, P. A.; Amenitsch, H.; Sanchez, C. Thermally Stable Nanocrystalline  $\gamma$ -Alumina Layers with Highly Ordered 3D Mesoporosity. *Angew. Chem., Int. Ed.* **2005**, *44*, 4589–4592.
- (15) Zhou, G.; Chen, Y.; Yang, J.; Yang, S. From Cylindrical-Channel Mesoporous Silica to Vesicle-Like Silica with Well-Defined Multilamella Shells and Large Inter-Shell Mesopores. *J. Mater. Chem.* **2007**, *17*, 2839–2844.
- (16) Kim, T.-W.; Kleitz, F.; Paul, B.; Ryoo, R. MCM-48-like Large Mesoporous Silicas with Tailored Pore Structure: Facile Synthesis Domain in a Ternary Triblock Copolymer–Butanol–Water System. *J. Am. Chem. Soc.* **2005**, *127*, 7601–7610.
- (17) Chen, D.; Li, Z.; Wan, Y.; Tu, X.; Shi, Y.; Chen, Z.; Shen, W.; Yu, C.; Tu, B.; Zhao, D. Anionic Surfactant Induced Mesophase Transformation to Synthesize Highly Ordered Large-Pore Mesoporous Silica Structures. *J. Mater. Chem.* **2006**, *16*, 1511–1519.
- (18) Baute, D.; Goldfarb, D. Interaction of Nitrates with Pluronic Micelles and Their Role in the Phase Formation of Mesoporous Materials. *J. Phys. Chem. C* **2007**, *111*, 10931–10940.
- (19) Guan, B.; Cui, Y.; Ren, Z.; Qiao, Z.; Wang, L.; Liu, Y.; Huo, Q. Highly Ordered Periodic Mesoporous Organosilica Nanoparticles with Controllable Pore Structures. *Nanoscale* **2012**, *4*, 6588–6596.
- (20) Warren, S. C.; Disalvo, F. J.; Wiesner, U. Nanoparticle-tuned Assembly and Disassembly of Mesostructured Silica Hybrids. *Nat. Mater.* **2007**, *6*, 156–161.
- (21) Bollmann, L.; Urade, V. N.; Hillhouse, H. W. Controlling Interfacial Curvature in Nanoporous Silica Films Formed by Evaporation-Induced Self-Assembly from Nonionic Surfactants. I. Evolution of Nanoscale Structures in Coating Solutions. *Langmuir* **2007**, *23*, 4257–4267.
- (22) Urade, V. N.; Bollmann, L.; Kowalski, J. D.; Tate, M. P.; Hillhouse, H. W. Controlling Interfacial Curvature in Nanoporous Silica Films Formed by Evaporation-Induced Self-Assembly from Nonionic Surfactants. II. Effect of Processing Parameters on Film Structure. *Langmuir* **2007**, *23*, 4268–4278.

- (23) Schubert, U.; Huesing, N.; Lorenz, A. Hybrid Inorganic–Organic Materials by Sol–Gel Processing of Organofunctional Metal Alkoxides. *Chem. Mater.* **1995**, *7*, 2010–2027.
- (24) Lichtenberger, R.; Schubert, U. Chemical Modification of Aluminium Alkoxides for Sol–Gel Processing. *J. Mater. Chem.* **2010**, *20*, 9287–9296.
- (25) Wang, Y.; Xu, M.; Peng, Z.; Zheng, G. Direct Growth Of Mesoporous Sn-doped TiO<sub>2</sub> Thin Films On Conducting Substrates for Lithium-Ion Battery Anodes. *J. Mater. Chem. A* **2013**, *1*, 13222–13226.
- (26) Wan, L.; Fu, H.; Shi, K.; Tian, X. Facile Synthesis of Ordered Nanocrystalline Alumina Thin Films with Tunable Mesopore Structures. *Microporous Mesoporous Mater.* **2008**, *115*, 301–307.
- (27) Vinu, A.; Gokulakrishnan, N.; Balasubramanian, V. V.; Alam, S.; Kapoor, M. P.; Ariga, K.; Mori, T. Three-dimensional Ultralarge-Pore Ia3d Mesoporous Silica with Various Pore Diameters And Their Application in Biomolecule Immobilization. *Chem.—Eur. J.* **2008**, *14*, 11529–11538.
- (28) Huang, J.; Tian, G.; Wang, H.; Xua, L.; Kan, Q. Large-pore Cubic Ia3d Mesoporous Silicas: Synthesis, Modification and Catalytic Applications. *J. Mol. Catal. A: Chem.* **2007**, *271*, 200–208.
- (29) Vinu, A.; Miyahara, M.; Hossain, K. Z.; Takahashi, M.; Balasubramanian, V. V.; Mori, T.; Ariga, K. Lysozyme Adsorption onto Mesoporous Materials: Effect of Pore Geometry and Stability of Adsorbents. *J. Nanosci. Nanotechnol.* **2007**, *7*, 828–832.
- (30) Jun, S.-H.; Lee, J.; Kim, B. C.; Lee, J. E.; Joo, J.; Park, H.; Lee, J.; Lee, S.-M.; Lee, D.; Kim, S.; Koo, Y.-M.; Shin, C. H.; Kim, S. W.; Hyeon, T.; Kim, J. Highly Efficient Enzyme Immobilization And Stabilization within Meso-Structured Onion-Like Silica for Biodiesel Production. *Chem. Mater.* **2012**, *24*, 924–929.
- (31) Kleitz, F.; Solovyov, L. A.; Anilkumar, G. M.; Choi, S. H.; Ryoo, R. Transformation of Highly Ordered Large Pore Silica Mesophases (*Fm*3*m*, *I*m3*m*, and *P*6*mm*) in a Ternary Triblock Copolymer–Butanol–Water System. *Chem. Commun.* **2004**, 1536–1537.
- (32) Kleitz, F.; Kim, T.-W.; Ryoo, R. Phase Domain of the Cubic Im3m Mesoporous Silica in the EO<sub>106</sub>PO<sub>70</sub>EO<sub>106</sub>–Butanol–H<sub>2</sub>O System. *Langmuir* **2006**, *22*, 440–445.
- (33) Zhao, D.; Feng, J.; Huo, Q.; Melosh, N.; Fredrickson, G. H.; Chmelka, B. F.; Stucky, G. D. Triblock Copolymer Syntheses of Mesoporous Silica with Periodic 50 To 300 Angstrom Pores. *Science* **1998**, *279*, 548.
- (34) Kleitz, F.; Liu, D.; Anilkumar, G. M.; Park, I.-S.; Solovyov, A.; Shmakov, A. N.; Ryoo, R. Large Cage Face-Centered-Cubic *Fm*3*m* Mesoporous Silica: Synthesis and Structure. *J. Phys. Chem. B* **2003**, *107*, 14296–14300.
- (35) Tayyari, S. F.; Milani-nejad, F. Vibrational Assignment of Acetylacetone. *Spectrochim. Acta Part A* **2000**, *56*, 2679–2691.
- (36) Nakamoto, K. *Infrared and Raman Spectra of Inorganic and Coordination Compounds*, 4th ed.; John Wiley & Sons, Inc.: USA, 1986; pp 27–120.
- (37) Bradley, D. C.; Mehrotra, R. C.; Gaur, D. P. *Metal Alkoxides*; Academic Press Inc. (London) Ltd.: 1978; pp 116–120.
- (38) Mehrotra, R. C.; Rai, A. K. Aluminium Alkoxides,  $\beta$ -Diketonates and Carboxylates. *Polyhedron* **1991**, *10*, 1967.
- (39) Manet, S.; Schmitt, J.; Impérator-Clerc, M.; Zholobenko, V.; Durand, D.; Oliveira, C. L. P.; Pedersen, J. S.; Gervais, C.; Baccile, N.; Babonneau, F.; Grillo, I.; Meneau, F.; Rochas, C. Kinetics of the Formation Of 2D-Hexagonal Silica Nanostructured Materials By Nonionic Block Copolymer Templating in Solution. *J. Phys. Chem. B* **2011**, *115*, 11330–11344.
- (40) Manet, S.; Lecchi, A.; Impérator-Clerc, M.; Zholobenko, V.; Durand, D.; Oliveira, C. L. P.; Pedersen, J. S.; Grillo, I.; Meneau, F.; Rochas, C. Structure of Micelles of A Nonionic Block Copolymer Determined By SANS and SAXS. *J. Phys. Chem. B* **2011**, *115*, 11318–11329.
- (41) Soni, S. S.; Brotons, G.; Bellour, M.; Narayanan, T.; Gibaud, A. Quantitative SAXS Analysis of the P123/Water/Ethanol Ternary Phase Diagram. *J. Phys. Chem. B* **2006**, *110*, 15157–15165.
- (42) Bergström, M. Derivation of Size Distributions of Surfactant Micelles Taking into Account Shape, Composition, and Chain Packing Density Fluctuations. *J. Colloid Interface Sc.* **1996**, *181*, 208–219.
- (43) Nelson, P. H.; Rutledge, G. C.; Hatton, T. A. On the Size and Shape of Self-Assembled Micelles. *J. Chem. Phys.* **1997**, *107*, 10777–10781.
- (44) Lettow, J. S.; Han, Y. J.; Schmidt-Winkel, P.; Yang, P.; Zhao, D.; Stucky, G. D.; Ying, J. Y. Hexagonal to Mesocellular Foam Phase Transition In Polymer-Templated Mesoporous Silicas. *Langmuir* **2000**, *16*, 8291–8295.
- (45) McDonagh, C.; Sheridan, F.; Butler, T.; MacCraith, B. D. Characterisation of Sol–Gel-Derived Silica Films. *J. Non-Cryst. Solids* **1996**, *194*, 72–77.
- (46) Tian, B.; Liu, X.; Tu, B.; Yu, C.; Fan, J.; Wang, L.; Xie, S.; Stucky, G. D.; Zhao, D. Self-Adjusted Synthesis of Ordered Stable Mesoporous Minerals By Acid–Base Pairs. *Nat. Mater.* **2003**, *2*, 159–163.
- (47) Zhao, D.; Huo, Q.; Feng, J.; Chmelka, B. F.; Stucky, G. D. Nonionic Triblock and Star Diblock Copolymer and Oligomeric Surfactant Syntheses of Highly Ordered, Hydrothermally Stable, Mesoporous Silica Structures. *J. Am. Chem. Soc.* **1998**, *120*, 6024–6036.
- (48) El-Safty, S. A.; Hanaoka, T.; Mizukami, F. Large-Scale Design of Cubic Ia3d Mesoporous Silica Monoliths with High Order, Controlled Pores, and Hydrothermal Stability. *Adv. Mater.* **2005**, *17*, 47–53.
- (49) Tolbert, S. H.; Landry, C. C.; Stucky, G. D.; Chmelka, B. F.; Norby, P.; Hanson, J. H.; Monnier, A. Phase Transitions in Mesostructured Silica/Surfactant Composites: Surfactant Packing and the Role of Charge Density Matching. *Chem. Mater.* **2001**, *13*, 2247–2256.
- (50) Zhao, D.; Wan, Y.; Zhou, W. *Ordered Mesoporous Materials*; Wiley-VCH Verlag GmbH & Co. KGaA: Weinheim, Germany, 2014; pp 73–74.